Influence of secular cooling on core-mantle boundary heat flux and mantle plume temperature over 1.8 billion years

Authors: Jiaxin Zhang[1,*], Nicolas Flament[1], Stéphane Labrosse[2], Xianzhi Cao[3], Dietmar Müller[4], Annalise Cucchiaro[1]

[1] Environmental Futures, School of Science, University of Wollongong, Wollongong, NSW 2522, Australia

[2] Laboratoire des sciences de la Terre, École Normale Supérieure de Lyon, Université de Lyon, CNRS UMR 5570, 46 Allée d'Italie, 69364 Lyon Cedex 07, France

[3] Frontiers Science Center for Deep Ocean Multispheres and Earth System, Key Lab of Submarine Geosciences and Prospecting Techniques, MOE and College of Marine Geosciences, Ocean University of China, Qingdao 266100, China

[4] EarthByte Group, School of Geosciences, the University of Sydney, NSW 2006, Australia

* Corresponding author

Email Address: jiaxinz@uow.edu.au

Abstract

Petrological evidence and global heat budgets indicate that the solid Earth has cooled substantially over geological time, yet the influence of secular cooling on mantle dynamics in global 3D models remains poorly quantified. We incorporate secular cooling into 3D global mantle flow models using plate reconstructions extending back 1.8 billion years. The core-mantle boundary (CMB) temperature is modelled as decreasing over time in scenarios consistent with continuous outer-core dynamo action and inner-core crystallization, while the internal heating rate declines with radiogenic isotopes decay. We find that secular cooling reduces the magnitude of CMB heat flow and globally averaged mantle plume temperature. The predicted global plume cooling rate (~110°C Gyr^{-1}) is broadly consistent with petrological evidence for secular plume cooling. The predicted plume heat flow at ~1,000 km depth (4–5.2 TW) is consistent with independent estimates from surface hotspots (2–4 TW), considering that lower-mantle plume heat flow is generally larger than upper-mantle plume heat flow. The CMB heat flux and the fractional area of Big LOwer-mantle Basal Structures (BLOBS) are strongly anti-correlated, reflecting that sinking slabs are central regulators of deep mantle heat transfer, with slab flux affecting deep mantle structure after a delay of 50–250 Myr. In the presented models, the evolution of the structure of the lower mantle is primarily controlled by the imposed plate reconstruction. However, secular cooling plays a second-order role as a decreasing plume flux and CMB heat flow result in a larger present-day African basal mantle structure that better matches tomographic models.

Keywords: mantle convection; secular cooling; core-mantle boundary; heat flow; mantle plume

Highlights

- We incorporate secular cooling in 3D global mantle flow models
- The models use a plate tectonic reconstruction extending back 1.8 billion years
- Secular cooling reduces plume temperature and CMB heat flow
- Sinking slabs regulate deep mantle heat transfer

1. Introduction

Global heat budgets and petrological evidence indicate that the bulk silicate Earth has been cooling over the past hundreds of millions of years. Current surface heat loss is between 43–49 TW, of which between 13–23 TW is supplied by radiogenic heating (e.g., Jaupart et al., 2015). Diverse estimates based on requirements to maintain dynamo action in Earth's outer core, mantle plume heat flux, and the thermal gradient of perovskite to post-perovskite phase transition (e.g., Labrosse and Jaupart, 2007; Lay et al., 2008; Nakagawa, 2020) suggest that the heat flow across the core-mantle boundary (CMB) accounts for between 5–17 TW of Earth's secular cooling, leaving between 1–29 TW of heat loss which is the secular cooling of the mantle (Fig. 1), which corresponds to a present cooling rate between 60–210 K Gyr^{-1}. Petrological studies further suggest that the Archaean mantle was ~100–300ºC hotter than today (e.g., Abbott et al., 1994; Grove and Parman, 2004) and that mantle plumes also cooled over time (Herzberg and Gazel, 2009). Komatiites, commonly interpreted to reflect high-temperature mantle melting and often linked to mantle plumes, further suggest elevated plume-source temperatures in the Archean (e.g., Grove and Parman, 2004).

The secular cooling of the solid Earth is the imbalance between total heat loss and energy generated within the planet (e.g., Jaupart et al., 2015). Although uncertain, secular cooling accounts for ~40% of Earth's total energy budget (Korenaga, 2006) and influences the long-term evolution of heat in Earth's core and mantle (e.g., Nakagawa, 2020; Nimmo, 2015).

Two important aspects of Earth’s secular cooling are the decrease in CMB temperature and internal heating rate. The vigour of mantle convection is expected to have decreased with CMB temperature throughout Earth’s history, and mantle potential temperature is expected to have decreased with internal heating rate (e.g., Li et al., 2023), cooling the mantle, and decreasing the effective Rayleigh number. Although the importance of secular cooling in mantle dynamics has long been recognized (e.g., Sharpe and Peltier, 1979; Nakagawa and Tackley, 2004; Li et al., 2023), secular cooling has not been included in global 3D mantle convection models driven by plate tectonic reconstructions. A recent study considered the time-dependence of internal heating but not the time-dependence of CMB temperature (O’Malley et al., 2024). The effect of secular cooling on global heat transfer and mantle dynamics becomes increasingly important in earlier geological times. Extending reconstructions of past plate motions from the past billion years (Merdith et al., 2021) to the past 1.8 Gyr (Cao et al., 2024) enables simulations of mantle convection and the effects of secular cooling over nearly 40% of Earth’s history. A coupled core-mantle thermal evolution model modified from Labrosse (2015) suggests that CMB temperature may have decreased by up to 12% from 1.8 Ga (Fig. S1b), potentially resulting in a significant effect on models of past mantle convection.

In this study, we carry out thermochemical mantle convection calculations driven by a plate motion history model extending back to 1.8 Ga (Cao et al., 2024) to investigate how a decreasing CMB temperature and a decreasing internal heating rate affect the secular variation of CMB heat flux, total plume heat flux, plume temperature, and the area of basal mantle structures or Big LOwer-mantle Basal Structures (BLOBS; Cucchiaro et al., 2025).

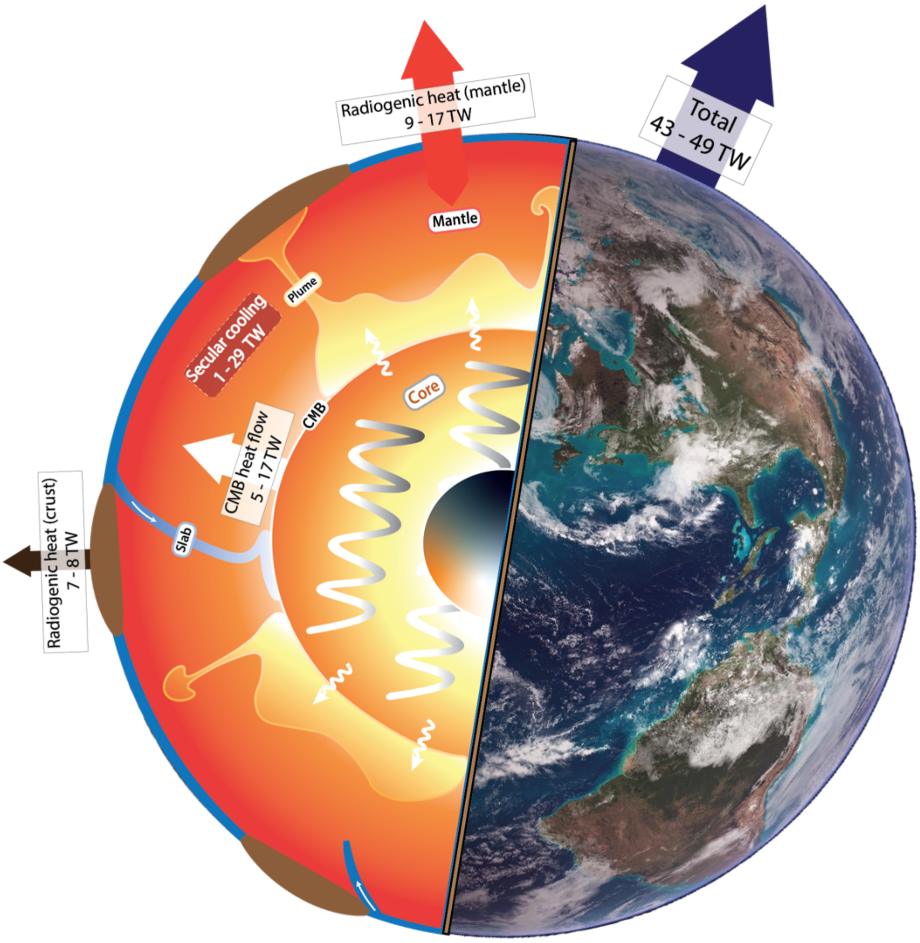

Figure 1. Schematic illustrating Earth's heat budget. The left semi-sphere illustrates dynamic processes in Earth's interior, including mantle and core convection. The global heat loss from the surface is between 43–49 TW, with between 9–17 TW due to radiogenic heat production from the mantle and between 1–29 TW due to present-day secular cooling (Jaupart et al., 2015). of secular cooling on global heat transfer and mantle dynamics becomes increasingly important in earlier geological times. Extending reconstructions of past plate motions from the past billion years (Merdith et al., 2021) to the past 1.8 Gyr (Cao et al., 2024) enables simulations of mantle convection and the effects of secular cooling over nearly 40% of Earth's history. A coupled core-mantle thermal evolution model modified from Labrosse (2015) suggests that CMB temperature may have decreased by up to 12% from 1.8 Ga (Fig. S1b), potentially resulting in a significant effect on models of past mantle convection.

2. Methods and setup

We implemented secular cooling in a version of the mantle convection code CitcomS (Zhong et al., 2008) modified to read in temperature boundary conditions from tectonic reconstruction models (Bower et al., 2015). We used CitcomS to solve the equations of conservation of mass, momentum, and energy under the extended Boussinesq approximation in a 3D spherical model domain. Under this approximation, viscous dissipation, an adiabatic temperature gradient, internal heating and a depth-dependent coefficient of thermal expansion are considered. Details of the governing equations can be found in Zhong (2008).

2.1 Paleogeographically constrained mantle flow models

We considered the plate tectonic reconstructions from Cao et al. (2024; called 'C24' hereafter), which is the first continuous global plate tectonic extending back to 1.8 Ga (nearly 40% of Earth's history). Reconstruction C24 was developed by integrating geological and geophysical data and spans the last three supercontinents (Nuna, Rodinia and Pangea), providing a tectonic framework to analyze long-term mantle convection. We considered reconstruction C24 in a no-net-rotation (NNR) and an optimized (OPT) reference frame (Fig. S2), both of which are appropriate to model mantle flow (Müller et al., 2022). The OPT reference frame was modified from the original paleomagnetic reference frame to minimise lithospheric net rotation, trench migration rate, and continental speed.

The models were formulated in a full spherical domain divided into 12 equal-volume caps, each consisting of 128 × 128 × 64 elements. The model was computed using 12 × 4 × 4 × 2 processors. The resolution was ~50 × 50 × 15 km near the surface and ~28 × 28 × 27 km near the CMB. The chemically distinctive basal mantle layer was initially laterally uniform and 113 km thick (2% of the volume of the mantle, Hernlund and Houser, 2008). The plate velocity, thermal structure of the lithosphere, and velocity and thermal structure of subducting slabs were assimilated progressively using a half-space cooling model in the convection models (Bower et al., 2015). A constant temperature $T = 15$ºC and time-dependent kinematic boundary conditions derived from plate motion history were imposed at the surface. The temperature was either constant or time-dependent at the free-slip CMB (see Section 2.2).

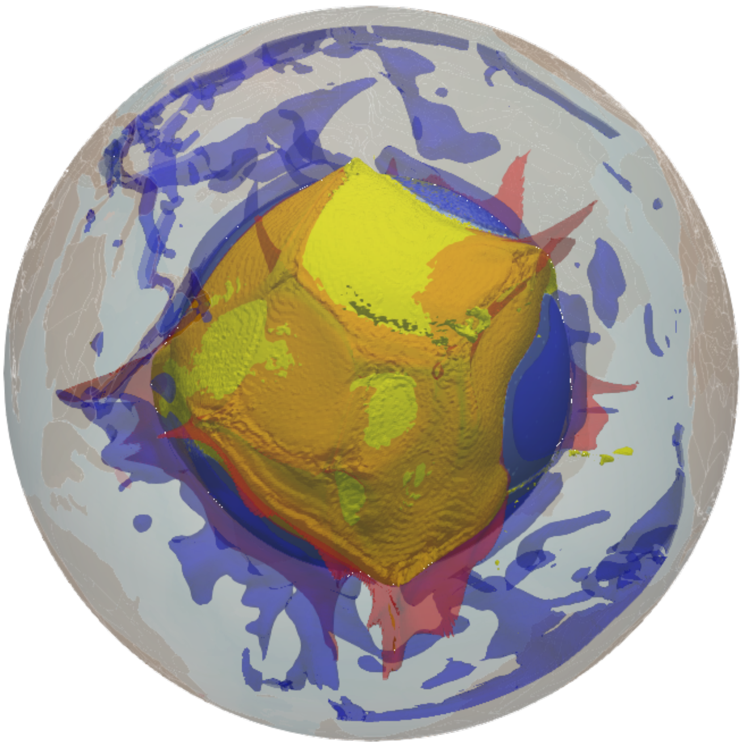

Figure 2. 3D snapshot of reference model case C-H_c at present-day centred on the Pacific BLOBS. At the surface, the transparent brown polygons with white outlines show continents. Blue and red iso-surfaces are 239 K colder-than-average and 409 K warmer-than-average, respectively. Golden regions show iso-surfaces of BLOBS tracer fraction ≥ 50%, with orange showing the overlap between BLOBS and hotter-than-average regions.

Convective vigour was controlled by the Rayleigh number $Ra = \frac{\rho g \alpha_0 \Delta T h^3}{\eta_0 \kappa}$, where ρ, α_0, η_0, κ were dimensional reference values for density, coefficient of thermal expansion, viscosity, and thermal diffusivity (Table 1). h was the thickness of the mantle. g was the gravitational acceleration. ΔT was the dimensional temperature change across the mantle, with the initial ΔT_{a_0} (a_0 = 1800 Ma) was used to scale temperature and define the initial *Ra* (Table 2). In secular cooling cases, ΔT decreased with time, decreasing the effective *Ra*. For the reference case, *Ra* was equal to 1.32×10^8.

Viscous dissipation was controlled by the dissipation number $Di = \frac{Rg\alpha_0}{C_P}$, where C_P was the reference heat capacity. The density contrast between the basal mantle material and background mantle was determined by the buoyancy number $B = \frac{\Delta\rho}{\rho_b \alpha_b \Delta T}$, where α_b was the average thermal expansivity in the deep mantle and $\frac{\Delta\rho}{\rho_b}$ was the relative intrinsic density contrast between the two materials. A buoyancy number equal to 0.375 represented basal mantle material ~1.6% denser than background mantle. As ΔT_{a_0} varied across models (Table 2), the intrinsic density contrast differed from the maximum by ~20% between cases.

Viscosity depended on depth, composition, temperature and pressure:

$$\eta = \eta(r)\eta_C exp\left\{\frac{E_\eta+\rho g Z_\eta(R-r)}{R_u(T+T_{\mathrm{off}})} - \frac{E_\eta+\rho g Z_\eta(R-R_C)}{R_u(T_{CMB}+T_{\mathrm{off}})}\right\},$$

where *r* was the radius, and the depth-dependent pre-factor was $\eta(r) = 1.4 \times 10^{19}$ Pa s above 160 km (lithosphere) and between 310–660 km depth, $\eta(r) = 4.3 \times 10^{17}$ Pa s between 160–310 km depth (asthenosphere), and $\eta(r) = 4.3 \times 10^{20}$ Pa s below 670 km depth (lower mantle). The compositional pre-factor η_C was equal to 100 for the continental lithosphere and equal to 10 for the basal layer. R_C was the radius of the core, E_η was the activation energy, R_u was the universal gas constant, Z_η was the activation volume, T was the dimensional temperature, $T_{\mathrm{off}} = 0.16\,\Delta T_{a_0}$ was a temperature offset, and ΔT_{a_0} was the initial temperature difference between the core-mantle boundary and the surface, which varied across models (Table 2). The effective viscosity was bounded by $0.1 \times \eta_0$ and $200 \times \eta_0$, corresponding to 7.16×10^{19}–1.43×10^{23} Pa s. Such lateral viscosity contrasts are lower than expected to occur within the solid Earth (Stadler et al., 2010), but they can be computed with a resolution that allows us to compute time-dependent mantle flow models. Model output was analysed in 20 Myr increment (see Fig. 2 for an example of the present-day temperature and composition).

Table 1. Fixed non-dimensional and dimensional model parameters.

Parameter	**Symbol**	**Value**
Reference thermal expansivity	α_0	3.0×10^{-5} K^{-1}
Basal thermal expansivity	α_b	1.32×10^{-5} K^{-1}
Density	ρ_0	4000 kg m^{-3}
Acceleration of gravity	g	9.81 m s^{-2}
Radius of the Earth	R	6371 km
Radius of the core	R_C	3504 km
Mantle thickness	h	2867 km
Heat capacity	C_P	1200 J kg^{-1} K^{-1}
Reference viscosity	η_0	7.16×10^{20} Pa s
Thermal diffusivity	κ	1×10^{-6} m^2 s^{-1}
Dissipation number	Di	0.71
Buoyancy number	B	0.375
Activation energy	E_η	284 kJ mol^{-1}
Universal gas constant	R_u	8.31 J mol^{-1}K^{-1}
Activation volume	Z_η	2.1×10^{-6} m^{3}mol^{-1}

Table 2. Parameters varied across model cases.

Model case	***a_0* (Ga)**	**Plates**	***H* (TW)**	**T_{CMB} (K)**	***Ra***	**ΔT_0 (K)**
C-H_c	1.8	C24OPT	constant	constant	1.32×10^8	3,409
C-H_t	1.8	C24OPT	H(t)	constant	1.32×10^8	3,409
S_{60}-H_t-Lo	1.8	C24OPT	H(t)	Self-consistent (60)	1.36×10^8	3,503
S_{90}-H_t	1.8	C24OPT	H(t)	Self-consistent (90)	1.29×10^8	3,338
S_{60}-H_t-Hi	1.8	C24OPT	H(t)	Self-consistent (60)	1.46×10^8	3,761
C-H_c-NNR	1.8	C24NNR	constant	constant	1.20×10^8	3,103
C-H_c-WU-NNR	2.05	C24NNR	constant	constant	1.20×10^8	3,103

2.2 Secular cooling

2.2.1 Core energy balance framework

To ascertain the effect of secular cooling, we implemented time-dependent CMB temperature (T_{CMB}) and internal heating rate *H* into the model. Time-dependent T_{CMB} was consistent with the CMB total heat flow according to a simplified core energy balance equation (e.g., Gubbins et al., 2003; Nimmo, 2015):

$$Q_{CMB} = -C\frac{dT_{CMB}}{dt}, \quad (1)$$

where *C* was the effective total heat capacity of the core, *t* was time, and $T_{CMB} = \Delta T + T_s$, where ΔT was the temperature difference across the mantle (input parameter into the mantle flow model) and T_s = 288 K was the assumed surface temperature.

2.2.2 Implementation of self-consistent T_{CMB}

In a core energy balance equation without radioactive heating the total heat flow across the CMB (Q_{CMB}) is proportional to the core cooling rate (e.g., Gubbins et al., 2003; Nimmo, 2015). We updated T_{CMB} using Eq. 1 with Q_{CMB} computed from the previous model timestep, so that T_{CMB} was self-consistent with Q_{CMB}: $T_{CMB\,(new)} = T_{CMB\,(old)} - \frac{Q_{CMB\,(old)}}{C}$, where 'new' indicated quantities at the current timestep and 'old' indicated quantities at the previous timestep.

The heat capacity of the core (e.g., Butler et al., 2005) increased significantly from the onset of inner core crystallization. The specific heat capacity by unit mass of the core is usually assumed to have been constant before inner core crystallization, ranging from 715 J kg^{-1} K^{-1} to 930 J kg^{-1} K^{-1} (see Nimmo, 2015, for a review). Multiplying the specific heat capacity by unit mass by the mass of the core (1.93×10^{24} kg), and converting seconds to million years, we obtained C $\simeq$ 60 TW Myr K^{-1} for the maximum effective total heat capacity of the core before inner core crystallization. Thermal evolution calculations for the core (Fig. S1a) suggest that *C* could be as large as 90 TW Myr K^{-1} after inner core crystallization. We used C = 60 TW Myr K^{-1} for most cases and considered a case (S_{90}-H_t) with C = 90 TW Myr K^{-1}.

2.2.3 Implementation of decreasing internal heating rate based on radiogenic decay

To examine the effect of secular cooling, we implemented a decreasing internal heating rate in the model (Fig. 3b) following the evolution of radiogenic heat production, defined as:

$$H(t) = H(0)\sum_{n=1}^{4} h_n exp(\lambda_n t),$$

where $H(0) = 13$ TW was the radiogenic heat production at present (Table 2), t was the time before present, h_n was the weighted heat generation rates of radiogenic isotopes according to their relative natural concentrations, and λ_n was the radioactive decay constant which described isotope decay rates (Table S1; Korenaga, 2006).

2.3 Considered model cases

Model case names consist of parts separated by hyphens: the first part indicates T_{CMB} to be either constant ('C'), or self-consistent ('S_{60}' for C = 60 TW Myr K^{-1} or 'S_{90}' for C = 90 TW Myr K^{-1}); the second part indicates H to be either constant (H_c) or time-dependent (H_t). Some models contain a third and/or fourth part to indicate additional model settings: 'WU' indicates a 250 Myr warm-up phase before the main calculation; 'NNR' indicates the no-net-rotation reference frame, and 'Lo' and 'Hi' indicate relatively lower and higher Ra, respectively (Table 2). If 'NNR' is not explicitly noted in the model case name, the model uses the optimized reference frame.

In the reference case (C-H_c), T_{CMB} and the internal heating rate H were constant. In C-H_t, T_{CMB} was constant (same as in C-H_c), while H decreased with time constant. The effect of the effective heat capacity of the core on the cooling rate can be inferred from cases S_{60}-H_t-Lo,

S_{60}-H_t-Hi, and S_{90}-H_t (Fig. 3a). The effect of a 250 Myr spin-up phase can be inferred from cases C-H_c-NNR and C-H_c-WU-NNR. The influence of the reference frame (OPT or NNR) can be inferred from cases C-H_c and C-H_c-NNR. *Ra* was adjusted (for example between S_{60}-H_t-Hi and S_{60}-H_t-Lo) so that models reached similar present-day CMB temperature (Fig. 3a).

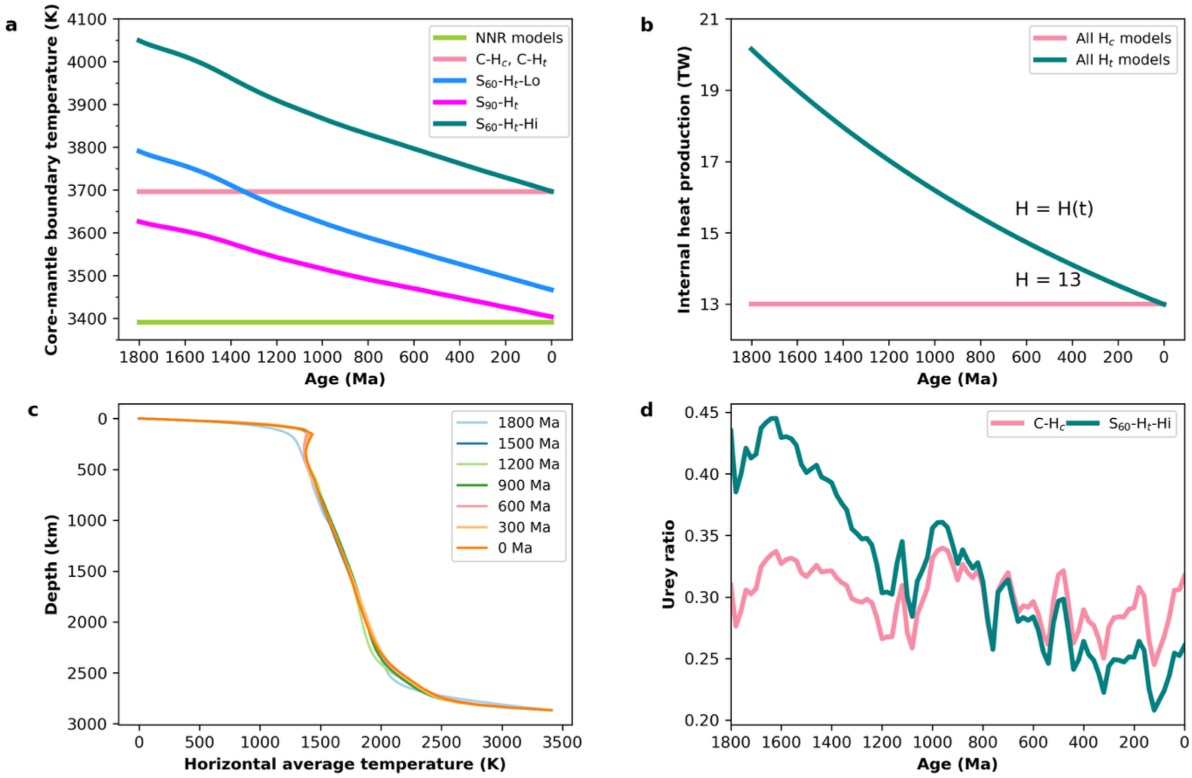

Figure 3. Secular cooling effects on evolution of CMB temperature, internal heating rate, and Urey ratio, with reference case temperature profiles. **a)** Evolution of CMB temperature, and **b**) evolution of internal heating across the considered model cases. **c)** Horizontally averaged temperature profiles through depth in case C-H_c, with profiles at different ages represented by different colours. **d)** Evolution of Urey ratio in cases C-H_c and S_{60}-H_t-Hi.

2.4 Quantifying model success

Match to tomography and volcanic eruptions. We computed the fractional area f_a as the surface-projected area of deep mantle regions covered by BLOBS (or LLSVPs), which were identified from two-means clustering (e.g., MacQueen, 1967) of temperature (or seismic velocity anomalies) between 1,000–2,800 km depth (e.g., Flament et al., 2022) in mantle flow models. We analysed four quantities to evaluate the fit of basal mantle structures to seismic tomographic models and volcanic eruption locations (Flament et al., 2022): (i) f_a; (ii) $\overline{Acc}$, the average spatial match between cluster maps of present-day BLOBS and LLSVPs imaged by seven global S-wave tomographic models: SEMUCB-WM1 (French and Romanowicz, 2014), Savani (Auer et al., 2014), S40RTS (Ritsema et al., 2011), GyPSuM-S (Simmons et al., 2010), S362ANI (Kustowski et al., 2008), SAW24B16 (Mégnin and Romanowicz, 2000), and HMSL-S (Houser et al., 2008).; (iii) $\overline{Sens}$, the average sensitivity between cluster maps of present-day BLOBS and LLSVPs imaged by seismic tomographic models, defined as $\overline{Sens} = \frac{TP}{(TP+FN)}$, where *TP* was the area of true positives and *FN* is the area of false negatives; (iv) $\overline{\theta}$, the time averaged mean of minimum angular distance between reconstructed volcanic eruption locations and BLOBS, with the distance considered equal to zero for eruption locations above BLOBS and positive for eruption locations outside BLOBS.

Evolution of plume flux. Following Labrosse (2002), Zhong et al. (2006) and Li et al. (2023), plumes were defined at each depth and time as regions with upward radial velocity where the temperature satisfied:$T \geq T_{bg} + f(T_{max} - T_{bg})$, where T_{bg} was the average temperature of hotter-than-average areas, T_{max} was the maximum temperature, f = 0.2 was a pre-factor. The total heat flux carried by plumes at a given depth and time was defined as: $Q_p = \int_S q_{\text{adv}} dS$ where S was the area of plumes that satisfied $T - T_{bg} \geq f(T_{max} - T_{bg})$, and q_{adv} was the convective heat flux, defined as: $q_{adv} = \rho C_p (T - T_{bg}) v_r$, where ρ and C_p were density and heat capacity, respectively, and v_r was the plume velocity in the radial direction. The globally averaged plume temperature was calculated at 1,040 km depth within plume regions defined above.

Urey ratio. The Urey ratio indicated the contribution of radiogenic heat production within the convecting mantle to the convective heat loss at the surface (Christensen, 1985):

$$Ur = \frac{H(t)}{Q(t)},$$

where Ur was the Urey ratio, $H(t)$ was the temporal mantle internal heating, and $Q(t)$ was the temporal convective surface heat loss. The Urey ratio provided insight into how Earth's interior cools over time. For the convecting mantle, Korenaga (2008) suggested a relatively low present-day convective Urey ratio of ~0.2 and a range between 0.2–0.3 over time, although broader mantle heat-budget estimates allow values of ~0.2–0.4 depending on assumptions about radiogenic heat production and convective heat loss (e.g., Jaupart et al., 2015)

2.5 Key characteristics of the tectonic forcing

To quantify the time-dependent tectonic forcing, we derived globally averaged spreading rate, convergence rate, and slab flux from the 1.8 Ga plate reconstruction following the plate-boundary statistics workflow of Müller et al. (2025). Relative plate motions were evaluated along divergent and convergent boundary segments. Spreading and convergence rates were calculated from the boundary-normal component of relative plate velocity across mid-ocean ridges and subduction zones, respectively, and averaged globally using plate-boundary segment weighting. Slab flux was calculated by multiplying convergence rate by trench length along subduction zones, providing a first-order estimate of the flux of oceanic lithosphere entering the mantle through time.

3. Results

3.1 Results for the reference case

For reference case C-H_c, the present-day surface heat flow was equal to 41.0 TW (Fig. 4a), which was consistent with the estimated heat flow from the convecting mantle excluding crustal radiogenic heat production (36–42 TW, Jaupart et al., 2015). The horizontally averaged mantle temperature at different depths varied by less than 4% over time (Fig. 3c), reflecting that the model evolved smoothly. The calculated present-day total heat flow across the CMB was equal to 15.2 TW (Fig. 4d), within the range of 5–17 TW estimated from core thermodynamics (Jaupart et al., 2015). It increased from 7.8 TW to 17.8 TW between 1.8–1.38 Ga, then gradually decreased to 15 TW and varied within 15% of 15 TW between 1.2–0 Ga, suggesting an approximate balance (‘dynamic equilibrium’) between internal heat production, surface heat loss, and basal heat flux. The computed present-day fractional area of BLOBS f_a was 37% (Fig. 4d), which was consistent with tomographic models (between 31.5% and 51.6%). f_a varied inversely with Q_{CMB}, decreasing between 1.8–1.4 Ga and then increasing toward quasi-equilibrium around 1.2 Ga. This anti-correlation was expected as Q_{CMB} is low through BLOBS, across which temperature gradients are relatively small. The anti-correlation between BLOBS area and CMB heat flow reflected the imposed tectonic history and model parameters including convective vigour and viscosity. In the reference case, Q_{CMB} reached dynamic equilibrium after ~800 Myr, following a ‘transient’ phase of large, opposite changes between Q_{CMB} and f_a (Fig. 4d). The Urey ratio averaged over time was equal to 0.29, reaching 0.32 at present day, which was close to the value range of 0.2–0.3 suggested by geochemistry (e.g., Korenaga, 2008). The Urey ratio varied between 0.24–0.33 by around 20% around its mean, reflecting that surface heat flow evolved over 1.8 Gyr (Fig. 3d). In contrast to the reference case, the Urey ratio decreased by ~40% over 1.8 Gyr in case S_{60}-H_t-Hi, because the internal heating rate declined while Q_{Surf} evolved dynamically (Fig. 3d).

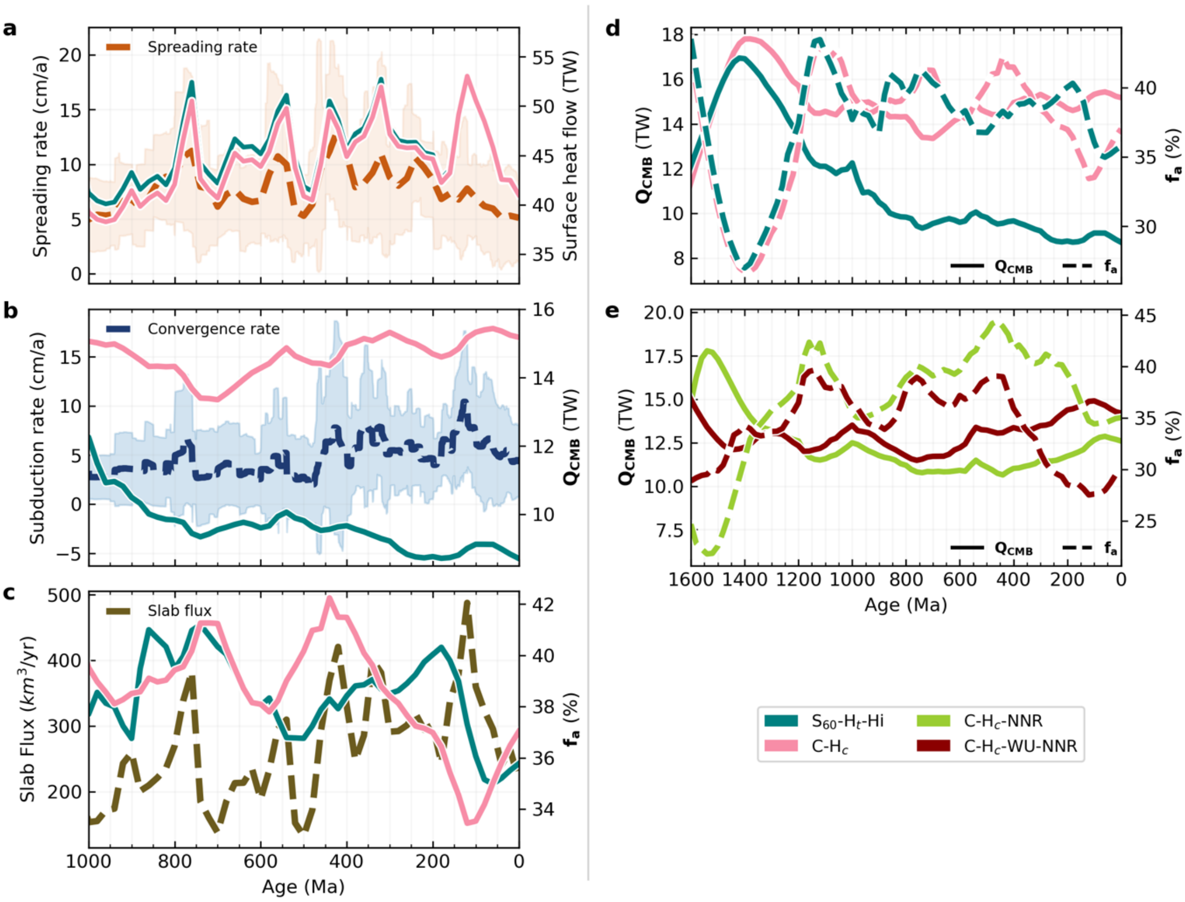

Figure 4. Temporal evolution of key characteristics of the tectonic reconstruction and mantle convection model. **a)** Spreading rate (orange dashed line) and surface heat flow as a function of time. **b)** Convergence rate (navy dashed line) and CMB heat flow Q_{CMB} as a function of time. **c)** Slab flux (olive dashed line) and BLOBS fractional area f_a as a function of time. In panels a–c, dashed lines represent quantities associated with the tectonic reconstruction, with shaded areas indicating uncertainty, and solid lines show model-predicted quantities, with colours indicating model cases (C-H$_c$ and S$_{60}$-H$_t$-Hi). **d)** Q_{CMB} and f_a for cases C-H$_c$ and S$_{60}$-H$_t$-Hi. **e)** Q_{CMB} and f_a for cases C-H$_c$-NNR and C-H$_c$-WU-NNR. In panels d-e, solid lines represent Q_{CMB}, and dashed lines represent f_a.

3.2 Effects of secular cooling on CMB heat flow and BLOBS area

The present-day CMB heat flow in model S_{60}-H_t-Hi was 37% lower than that in the reference case (Fig. 4d), although they reached a similar present-day CMB temperature (Fig. 3a). This is because basal secular cooling decreases the temperature gradient in the lower mantle over time (Fig. 5), reducing Q_{CMB}. Indeed, the horizontally averaged temperature at different depths were similar in the initial condition but the lowermost mantle was cooler at present-day in models with basal secular cooling (Fig. 5a, b). On the other hand, the present-day Q_{CMB} in model C-H_t, which only considered cooling from the interior (Fig. S3c), was similar to that in C-H_c, reflecting that basal cooling had a larger effect than internal cooling on the magnitude of Q_{CMB}. As in reference model C-H_c, Q_{CMB} increased when f_a decreased in all models with secular cooling (Figs 5d, e and S2), although with a reduced Q_{CMB} magnitude in models with basal secular cooling.

Analysing the input tectonic reconstruction revealed that periods of increased convergence and slab flux were followed by increased Q_{CMB} and decreased f_a after a time delay of ~50–250 Myr (Fig. 4b, c). In contrast, surface heat flow broadly followed variations in spreading rate (Fig. 4a), which was expected because the thermal structure of the oceanic lithosphere was imposed in our models as a function of lithospheric age, which controlled heat flux (e.g., Parsons and Sclater, 1977).

Increasing C from C $\simeq$ 60 TW Myr K^{-1} (S_{60}-H_t-Lo) to C $\simeq$ 90 TW Myr K^{-1} (S_{90}-H_t) decreased the CMB cooling rate from 180 K Gyr^{-1} to 123 K Gyr^{-1} (Fig. 3a) and increased Q_{CMB} by ~15% (Fig. S3a). Increasing convective vigour increased the cooling rate, as expected. The cooling rate was 180 K Gyr^{-1} for case S_{60}-H_t-Lo and 196 K Gyr^{-1} for case S_{60}-H_t-Hi (Fig. 3a). For these two cases, the present-day T_{CMB} was equal to 3,467 K (case S_{60}-H_t-Lo) and to 3,697 K (case S_{60}-H_t- Hi), respectively. T_{CMB} and Q_{CMB} were ~9.5% greater in model S_{60}-H_t-Hi than in model S_{60}-H_t-Lo for all times (Fig. 3a and Fig. S3b).

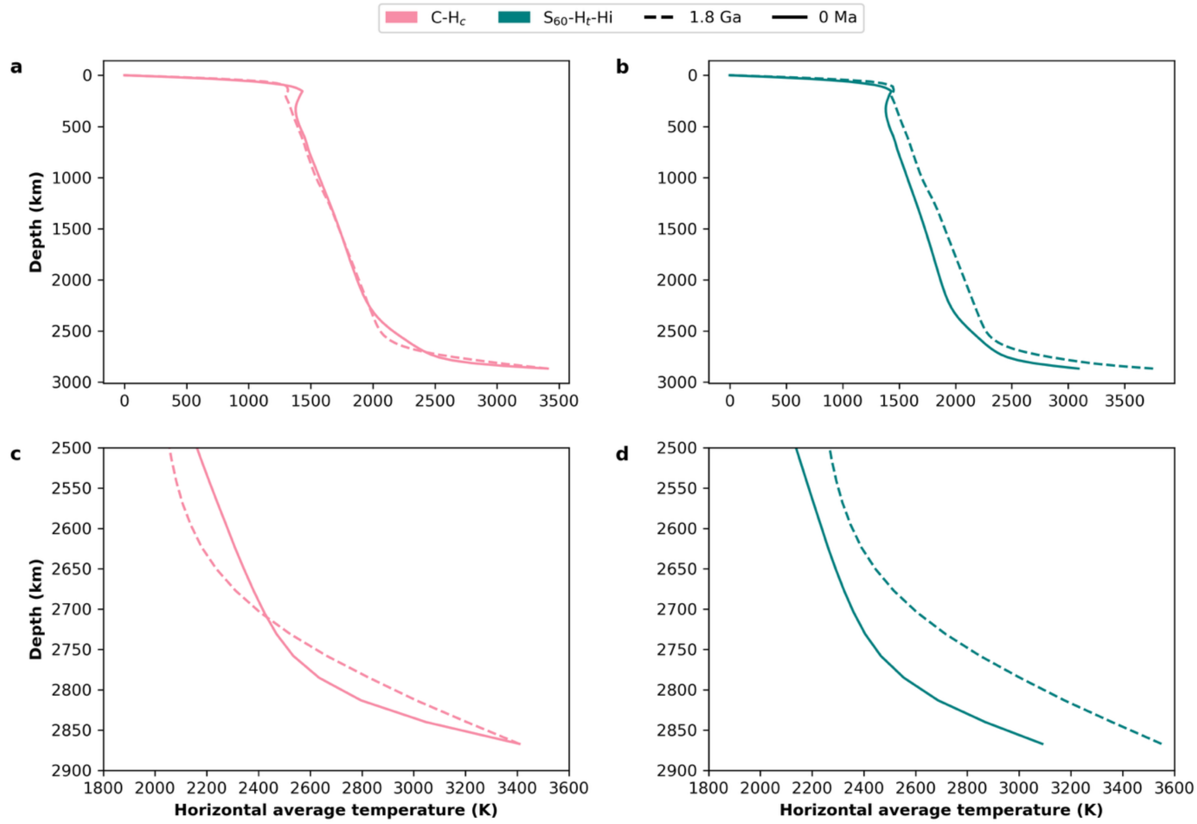

Figure 5. Evolution of dimensional horizontal average temperature (in the initial condition and at the present-day) for models C-H$_c$ (**a** and **c**), and S$_{60}$-H$_t$-Hi (**b** and **d**). **c** and **d** show zoomed views of the lowermost mantle depths. The initial temperature profiles are very similar across all models.

3.3 Effect of a warm-up phase on the initial transient adjustment

As in the reference case, all models without a warm-up phase showed an initial transient phase of ~ 800 Myr before Q_{CMB} and f_a reached its quasi-equilibrium, regardless of whether secular cooling was applied. To evaluate the duration of this transient phase, we compared two NNR cases with or without a 250 Myr warm-up phase. The warm-up phase shifted the early Q_{CMB} peak by ~250 Myr and reduced the amplitude of the initial adjustment, but it did not eliminate the transient phase (Fig. 4e).

3.4 Evaluating model success

We evaluated model success and parameter trade-offs from f_a, $\overline{Acc}$, $\overline{Sens}$, and $\bar{\theta}$ (see Section 2.7). For tomographic models, the fractional area was $0.32 < f_a < 0.52$, with median f_a equal to 0.34 (Fig. 6a). For mantle flow models, it was $0.3 < f_a < 0.4$ for all cases and f_a fell outside the tomographic range only for the reference case C-H_c-WU-NNR ($f_a = 0.3$) (Fig. 6a). f_a was closer to the median of tomographic models for models using reconstructed plate history extending back to 1.8 Ga.

The accuracy was $0.73 < \overline{Acc} < 0.88$ across tomographic models, with median $\overline{Acc}$ = 0.83 (Fig. 6b). A large accuracy indicates a good match between a given model and all considered tomographic models. For mantle flow models $\overline{Acc}$ ranged from 0.68 to 0.76, with cases S_{60}-H_t-Hi, and C-H_c-WU-NNR falling within the range of tomographic models (Fig. 6b). However, the accuracy for the mantle flow models was generally lower than the median value of tomographic models (Fig. 6b).

The sensitivity was $0.62 < \overline{Sens} < 0.82$ for tomographic models, with the median $\overline{Sens} = 0.77$ (Fig. 6c). Larger sensitivities indicated a better spatial match between BLOBS and LLSVPs for a given model and tomographic models. For the mantle flow models, sensitivity ranged from 0.55 to 0.63, and was generally lower than the tomographic range, except for case C-H_c-WU-NNR ($\overline{Sens}$=0.630) (Fig. 6c). In the models with secular cooling, sensitivity was the largest for case S_{60}-H_t-Hi.

The time-averaged mean distance from volcanic eruptions to BLOBS was $2.80° < \bar{\theta} < 9.32°$ across tomographic models, with the median equal to 6.73° (Fig. 6d). Smaller time-averaged mean distance from volcanic eruptions indicated models that were most consistent with volcanic eruptions, assuming a link between BLOBS or LLSVPs and surface volcanic eruptions (Torsvik et al., 2010; Flament et al., 2022; Müller et al., 2022; Cucchiaro et al., 2025). This range was larger for the mantle flow models ($6.81° < \bar{\theta} < 13.63°$, Fig. 6d). The average angular distance for cases S_{60}-H_t-Lo, C-H_c, C-H_t, and S_{60}-H_t-Hi, was within 1° from the median for tomographic models.

Case S_{60}-H_t-Hi was the mantle flow model that provided the best joint fit to tomography and surface volcanism. This could be verified by the similarity between the cluster maps (1,000-2,800 km depths) for case S_{60}-H_t-Hi and tomographic models at 320 million years ago and at present-day (Fig. S4).

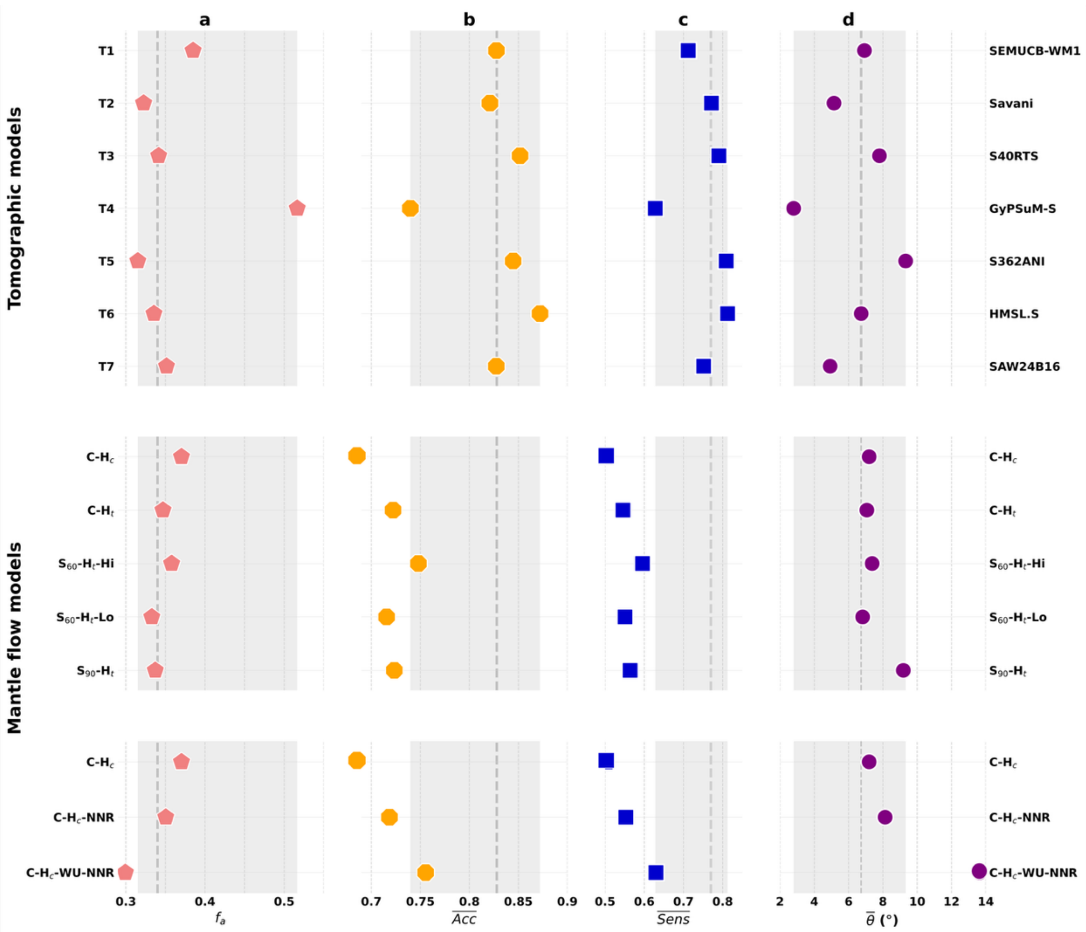

Figure 6. Fit of basal mantle structures from global mantle flow models to seismic tomography models and volcanic eruption locations. **a)** f_a fractional area of deep mantle cluster maps between 1,000 km and 2,800 km depths covered by slow (in tomography) or hot (at present-day in mantle flow models) basal mantle structures. **b)** $\overline{Acc}$**,** averaged spatial match between present-day basal mantle structures for a given model and tomographic models T1-T7. **c)** $\overline{Sens}$, averaged sensitivity of present-day basal mantle structures for a given model to tomographic models T1-T7. **d)** $\bar{\theta}$, mean of minimum angular distance averaged from 320 Ma between volcanic eruption locations and basal mantle structures edges. The top panel presents results across tomographic models T1-T7, and the middle and bottom panel exhibits results for global mantle flow models investigated in this study. Grey shaded areas marked the range of metrics for tomographic models T1-T7 (for $\overline{Acc}$ and $\overline{Sens}$, independent tomographic models are considered). Grey dashed lines indicated the median of metrics for tomographic models T1-T7.

3.5 Temporal evolution of plume heat flow and plume temperature

We analysed the temporal variation of the global-averaged plume temperature and total heat flux carried by plumes (defined in Section 2.4) at 1,040 km depth (Fig. 7a). We compared the predictions for cases C-H_c and S_{60}-H_t-Hi. In both cases, after the transient phase (at ~ 1.2 Ga), the plume heat flow increased gradually until reached a relatively stable stage between 400–0 Ma (Fig. 7a). Absolute plume heat flux was generally lower in S_{60}-H_t-Hi than in C-H_c for the last 400 Myr (Fig. 7a). Results for model cases with and without basal cooling were generally similar to cases S_{60}-H_t-Hi and C-H_c, respectively, with some second-order differences (Fig. S5). This suggests that the imposed plate reconstruction controlled the first-order evolution of plume heat flux. Plume heat flow averaged ~4 TW in secular cooling cases and 5.2 TW in C-H_c from 400 Ma to the present-day (Fig. S5a). Normalized to CMB heat flow, plumes carried 35–45% of present-day core heat flow and 40–50% on average over the past 400 Myr in the secular-cooling cases, compared with ~40% and ~35%, respectively, in C-H_c (Figs. 8c, S5b), which was within the range estimated in previous numerical studies (e.g., Mittelstaedt and Tackley, 2006; Arnould et al., 2020). Over 1.8 Gyr, lower mantle plumes carried, on average, 32% of the CMB heat flow in the secular cooling case S_{60}-H_t-Hi, compared with only 26% in the constant heating case C-H_c (Fig. 7b). From ~1 Ga, the normalized plume flow in case S_{60}-H_t-Hi was larger than that in case C-H_c (Fig. 7b).

Global mean plume temperature was relatively stable in C-H_c, but decreased toward the present day in S_{60}-H_t-Hi (Fig. 7c). During the quasi-equilibrium phase, the plume temperature in S_{60}-H_t-Hi decreased at a rate of ~110°C Gyr^{-1} from 1.2 Ga (after the transient phase). This decrease, which is broadly consistent with petrological evidence (Herzberg and Gazel, 2009), was not observed in the constant heating reference case, as expected.

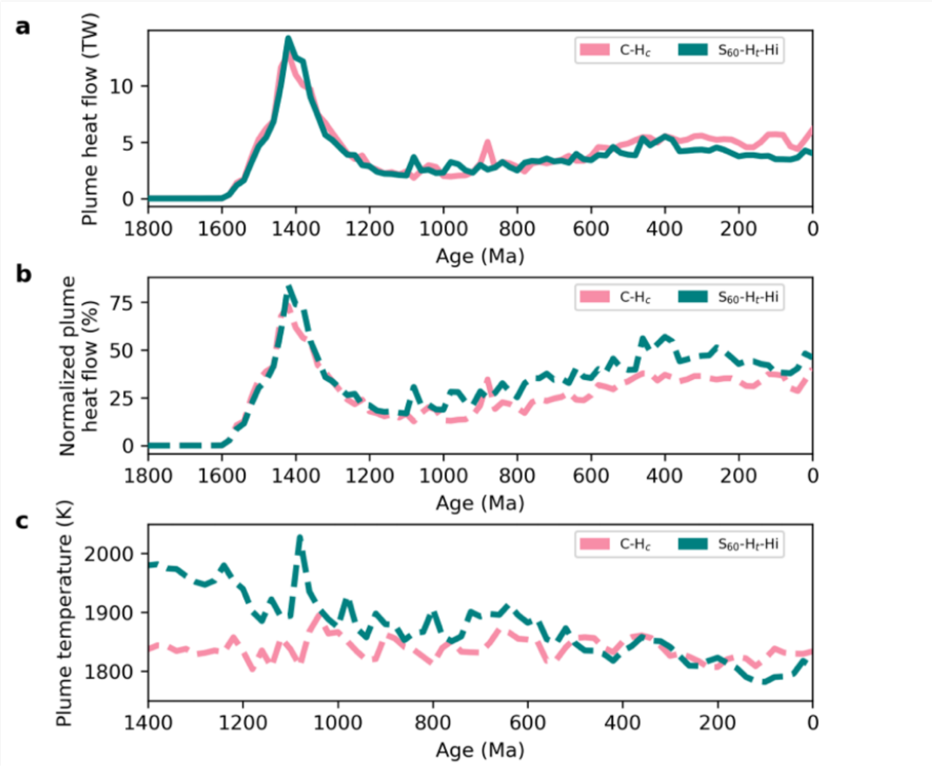

Figure 7. Evolution of plume heat flux and plume temperature predicted by mantle flow models. **a)** Heat flux carried by lower mantle plumes at 1,040 km depth, Q_p, for model cases C-H$_c$ and S$_{60}$-H$_t$-Hi. Plume flux is represented by solid lines, with pink indicating the model with constant heating and teal indicating a secular cooling case. **b)** Plume heat flux at 1,040 km depth normalized to CMB heat flow, for model cases C-H$_c$ and S$_{60}$-H$_t$-Hi. **c)** Global mean plume temperature through time, represented by dashed lines, for cases C-H$_c$ and S$_{60}$-H$_t$-Hi, calculated at 1,040 km depth.

4. Discussion

Our models consistently showed a ~800 Myr transient phase during which the CMB heat flux increased sharply as slabs reorganized and deformed the basal thermochemical layer, after which the system relaxed toward a quasi-steady thermal regime. In our models, the duration of the initial transient phase was expected to depend on convective vigour (Rayleigh number), viscosity, initial condition (initial slab depth, presence of a dense basal layer) and the tectonic reconstruction. Considering a 250 Myr warm-up phase shifted the early CMB heat-flow peak by ~250 Myr but did not eliminate the transient phase (Fig. 4e). This indicates that the transient phase reflects not only slab transit across the mantle, but also the time required for slabs to reorganize the lowermost mantle thermal structure. The duration of the transient phase should therefore be characterised, and the period overlapping with this transient phase should be ignored when interpreting the results of forward global mantle flow models. The duration of the transient phase depends on the model setup. For example, it was ~50 Myr long for one model case with a dense basal layer and > 200 Myr long for a model case without dense basal layer in models by Flament et al. (2014) that did not account for secular cooling, dissipation, or an adiabatic gradient.

The anti-correlation between CMB heat flux and the fractional area of BLOBS is a robust and persistent feature across all models. As mantle downwelling then slabs impinge on the basal thermochemical layer, BLOBS are compressed and displaced, reducing their area and increasing CMB heat flow. This response is driven by the tectonic forcing but delayed: convergence rate and slab flux are reflected in Q_{CMB} and f_a ~50-250 Myr after slabs started subducting, reflecting a delay linked to slab sinking (e.g., van der Meer et al., 2010) (Figs. 6b–c). This finding contrasts with a previous who suggestion that variations in surface RMS velocities and CMB heat flux could be synchronous (Zhang and Zhong, 2011). The relationship between BLOBS and CMB heat flux is consistent with earlier 2D and 3D thermochemical models showing that the geometry of dense basal structures strongly modulates deep-mantle heat transfer (e.g., Nakagawa and Tackley, 2004; Li et al., 2018; Nakagawa and Tackley, 2008). In 3D spherical geometry, these interactions are inherently more complex than in reduced-dimensional models, producing a dynamic interplay among slabs, BLOBS margins, and plume initiation zones.

Deep-time plate reconstructions are very uncertain as they are only constrained by known paleomagnetic poles and tectonic events preserved on the continents (Cao et al., 2024). This uncertainty is compounded by the decrease in preserved continental area back in time, down to ~60% at 1.8 Ga (e.g., Dhuime et al., 2017), with the consequence that the subduction girdle surrounding assembled continents is tighter at 1,800 Ma than at 900 Ma (Fig. S2), which could contribute to the long initial transient phase in the considered models. Reconstruction C24 is currently the only continuous global reconstruction extending back to 1.8 Ga, limiting the sensitivity analysis to considering alternative reference frames (OPT and NNR) for mantle convection modelling. This uncertainty is significant given that the imposed plate reconstruction exerts a first-order control on the temporal evolution of deep mantle structures and heat transfer, whereas secular cooling modifies the amplitude of CMB heat flux.

The secular cooling cases consistently generally yielded a larger $\overline{Acc}$, a larger $\overline{Sens}$ and a slightly smaller present-day f_a than the constant heating case C-H_c (Fig. 6a, b, c). The slightly smaller present-day f_a in models with secular cooling reflected that secular cooling reduced plume heat flow by about 20% from 600 Ma (Fig. 7a), promoting stronger entrainment of BLOBS material into plumes and enhanced BLOBS erosion (Bodur and Flament, 2023) in models without secular cooling. A rapid decrease in the area of basal mantle structures between 400–100 Ma was predicted for C-H_c but not for S_{60}-H_t-Hi (Fig. 4c), because f_a was anti-correlated with Q_{CMB} (Fig. 4d,e) and Q_{CMB} was larger in C-H_c than in S_{60}-H_t-Hi from ~1 Ga (Fig. 4d). This decrease in f_a for C-H_c reflected an increased slab flux from ~700 Ma (Fig. 4c) that was particularly large in the African hemisphere (Fig. S2 and Flament et al., 2022). The predicted African structure was larger and a better match to the Savani LLSVP in S_{60}-H_t-Hi than in C-H_c (Fig. 8), with an intermediate match for C-H_t (Fig. 6) suggesting that the structure of the lower mantle depends on basal secular cooling more than on secular cooling from the interior. While a different set of parameters could have led to a model without secular cooling better fitting tomographic constraints than a model with secular cooling, the result illustrates that secular cooling plays a second-order role in shaping the predicted deep mantle structure.

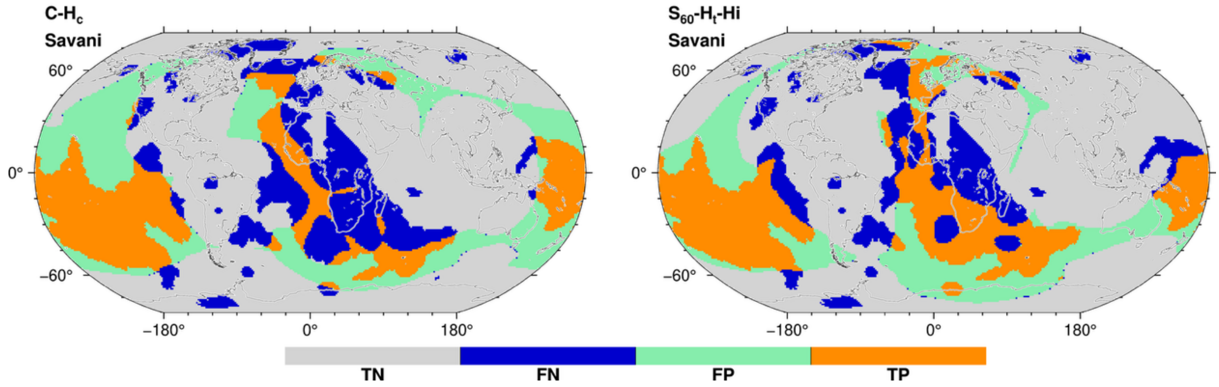

Figure 8. Spatial match of lower mantle structure predicted by mantle flow models (C-H_c and S_{60}-H_t-Hi) and tomographic model Savani (Auer et al., 2014) at present-day. Intersections of mantle structure revealed by *k*-means cluster analysis between 1,000 km and 2,800 km for tomographic model Savani and mantle flow models with and without secular cooling at present day. Orange (true positive, 'TP') indicates high-temperature (or low-velocity) regions and low-velocity tomographic regions, grey (true negative, 'TG') indicates low-temperature (or high-velocity) regions and high-velocity tomographic regions, green (false positive, 'FP') indicates high-temperature (or low-velocity) regions and high-velocity tomographic regions and blue (false negative, 'FN') indicates low-temperature (or fast-velocity) regions and low-velocity tomographic regions.

Our models do not exhibit the quasi-periodic plume pulses observed in many 2D models (e.g., Lin and van Keken, 2005; Olson and Amit, 2015; Li et al., 2018; Heyn et al., 2020). In simplified 2D geometries with free-slip vertical boundaries, slabs descend along the sides of the model domain, forcing plume formation directly above the crest of BLOBS and producing regular oscillatory patterns. In contrast, in 3D spherical models – whether ours or previous studies (Li et al., 2014; McNamara and Zhong, 2004; Hassan et al., 2015; Tan et al., 2011; Cao et al., 2021; Cucchiaro et al., 2025) – plumes can originate above, along, or near BLOBS margins. This geometric freedom suppresses simple thermal resonance behaviour and yields spatially and temporally heterogeneous plume production. Li et al. (2023) further showed that plume periodicities decrease with increasing convective vigour in 3D global convection models, consistent with our finding that decreasing CMB temperature influences the variance of plume activity by reducing convective vigour.

Plume temperature provides an additional diagnostic of how secular cooling affects plume dynamics. In the secular-cooling case, global average plume temperature decreases by

~110°C/Gyr, whereas the constant-heating case shows a stable plume temperature over time (Fig. 7c). The plume temperature decrease was smaller than the CMB temperature decrease over time, reflecting that the imposed cooling was greatest at the base of the mantle, affecting both the adiabat with a convection timescale and the temperature gradient in the basal thermal boundary layer with a diffusion timescale. This behaviour is qualitatively consistent with petrological evidence for a hotter mantle in the past, including komatiite-based interpretations of elevated Archaean mantle or plume-source temperatures and secular mantle cooling (e.g., Abbott et al., 1994; Grove and Parman, 2004). A petrological estimate for plume magmatism also suggests secular plume cooling, from ~1560–1620°C in the Cretaceous to ~1500°C at present (e.g., Herzberg and Gazel, 2009), although this is much faster than the secular cooling rate inferred from komatiites or predicted by our models. This could reflect that the estimates by Herzberg and Gazel (2009) were for the source potential temperatures of individual plume systems, whereas we computed the global average temperature of plume regions at 1,040 km depth. The predicted plume-temperature evolution therefore provides a model-based measure of how decreasing T_{CMB} and internal heating affects plume thermal state, rather than a direct prediction of petrological source temperatures.

Our modelling framework incorporates a simplified coupling between mantle convection and core energy balance. Unlike more complex formulations (e.g., Nakagawa and Tackley, 2004; Nakagawa and Tackley, 2012), we do not include the onset of inner-core growth or latent heat and gravitational energy release associated with solidification. These additions influence effective core heat capacity but also introduce significant uncertainties in material properties of the deep core. Besides, when assimilating slabs following the method of Bower et al. (2015), the CMB temperature was assumed to be constant (mean of the present-day and 1.8 Ga) and not updated over time. This may have modestly enhanced mantle circulation and plume flux initially and slightly reduced them later. However, because CMB temperature varied by only ~5% around the applied mean (Fig. 3a), the effect on slab temperature and first-order results is negligible. Despite these simplifications, the cooling rates produced by our models (~123–198 K Gyr^{-1}) fell within the range estimated from Earth's Urey ratio and convective heat flux (Korenaga, 2008) and overlapped the broader range inferred for secular cooling (60–210 K Gyr^{-1}). Although our rates were slightly higher than some geodynamic estimates (e.g., Zhong, 2006; Nakagawa and Tackley, 2004; Nakagawa and Tackley, 2012) and exceeded values inferred from geological proxies (e.g., Abbott et al., 1994; Grove and Parman, 2004; Nisbet and Fowler, 1983), they were consistent with first-order constraints. In addition, our predicted heat flow carried by plumes at 1,040 km depth (4–5.2 TW) broadly match with, although 1.5–2 times larger than the previous estimates of 2–4 TW from buoyancy of hotspots swells (e.g., Davies, 1988; Sleep, 1990). This is expected because lower mantle plume flux may be ~1.5 times larger than the upper mantle plume flux (Arnould et al., 2020), and possibly greater than surface plume flux inferred from hotspot swells. Our prediction of ~4–5 TW was therefore reasonable. Although the plumes in our model carried slightly smaller portion of the CMB heat flow compared to a recent study (Arnould et al., 2020), the normalized plume flux can have a wide range, depending on convective vigour, temperature dependence of viscosity, and internal heating rate (e.g., Mittelstaedt and Tackley, 2006).

Overall, our results demonstrate that plate-driven slab–BLOBS interactions exert a first-order control on the evolution of deep mantle structures, while secular cooling modifies the deep mantle thermal state, amplitude of CMB heat flow and plume temperature. Future studies can expand on this framework, for example by incorporating a more sophisticated model of the thermal evolution of the core including inner-core growth (e.g., Nakagawa and Tackley, 2004), or ridge melting and dehydration effects (e.g., Korenaga, 2017).

5. Conclusions

1. Secular cooling should be included in long-term global mantle flow models. Our 3D global thermochemical convection models incorporating 1.8 billion years of plate motion history demonstrate that secular basal cooling reduces the magnitude of CMB heat flow and long-term temperature of plumes, and plays a second-order role in shaping the structure of the lower mantle. By explicitly coupling mantle convection with a time-dependent CMB temperature and declining internal heating, we show that secular cooling lowers Q_{CMB} by over 30% than models with constant heating conditions; global plume temperature cools by ~110°C/Gyr, whereas plumes do not cool in models with constant heating conditions.

2. Tectonically-driven slabs–BLOBS interactions regulate CMB heat flux. The consistent anti-correlation between CMB heat flow and BLOBS area across all models indicates that the deformation and movement of basal thermochemical structures strongly modulate heat transfer from the core. The imposed plate reconstruction controls the timing and pattern of this interaction through subduction activities, with changes CMB heat flux and basal structure area lagging changes in slab flux by ~50–250 Myr.

3. All simulations consistently feature an extended transient phase during which sinking slabs and the deformation of basal thermochemical structures act to reorganize deep mantle flow before a long-term dynamic equilibrium is established.

4. Overall, our results show that although slab sinking exerts a first-order control on the temporal evolution of deep mantle heat transfer, secular cooling affects long-term plume temperature, CMB heat flux, and plays a second-order role in shaping the structure of the deep Earth. Future improvements could consist of incorporating inner-core growth and upper-mantle dehydration effects.

Acknowledgments

Jiaxin Zhang and Nicolas Flament were supported by Australian Research Council (ARC) grant LP220100056 (industry partners: Anglo American and De Beers). Nicolas Flament was supported by ARC FT230100001. The models were performed using computational resources on the National Computational Infrastructure (NCI), which is supported by the Australian Government. Access to NCI was partly supported by resources and services from the University of Wollongong (UOW).

CRediT authorship contribution statement

Jiaxin Zhang: Conceptualization, Investigation, Methodology, Software, Visualization, Analysis, Writing – original draft, Writing – review and editing. **Nicolas Flament:** Conceptualization, Methodology, Analysis, Writing – review and editing, Supervision, Project administration, Funding acquisition. **Stéphane Labrosse:** Methodology, Writing – review and editing, **Xianzhi Cao:** Methodology, Writing – review and editing. **Dietmar Müller:** Methodology, Writing – review and editing. **Annalise Cucchiaro:** Visualization, Writing – review and editing.

References

1. Abbott, D., Burgess, L., Longhi, J., & Smith, W. H. F. (1994). An empirical thermal history of the Earth's upper mantle. *Journal of Geophysical Research: Solid Earth*, *99*(B7), 13835-13850. https://doi.org/10.1029/94jb00112
2. Arnould, M., Coltice, N., Flament, N., & Mallard, C. (2020). Plate tectonics and mantle controls on plume dynamics. *Earth and Planetary Science Letters*, *547*, 116439. https://doi.org/10.1016/j.epsl.2020.116439
3. Auer, L., Boschi, L., Becker, T., Nissen-Meyer, T., & Giardini, D. (2014). Savani: A variable resolution whole-mantle model of anisotropic shear velocity variations based on multiple data sets. *Journal of Geophysical Research: Solid Earth*, *119*(4), 3006-3034. https://doi.org/10.1002/2013JB010773
4. Bodur, Ö. F., & Flament, N. (2023). Kimberlite magmatism fed by upwelling above mobile basal mantle structures. *Nature Geoscience*, *16*(6), 534-540. https://doi.org/10.1038/s41561-023-01181-8
5. Bower, D. J., Gurnis, M., & Flament, N. (2015). Assimilating lithosphere and slab history in 4-D Earth models. *Physics of the Earth and Planetary Interiors*, *238*, 8-22. https://doi.org/10.1016/j.pepi.2014.10.013
6. Butler, S., Peltier, W., & Costin, S. (2005). Numerical models of the Earth’s thermal history: Effects of inner-core solidification and core potassium. *Physics of the Earth and Planetary Interiors*, *152*(1-2), 22-42. https://doi.org/10.1016/j.pepi.2005.05.005
7. Cao, X., Flament, N., Bodur, O. F., & Muller, R. D. (2021). The evolution of basal mantle structure in response to supercontinent aggregation and dispersal. *Sci Rep*, *11*(1), 22967. https://doi.org/10.1038/s41598-021-02359-z

8. Cao, X. Z., Collins, A. S., Pisarevsky, S., Flament, N., Li, S. Z., Hasterok, D., & Müller, R. D. (2024). Earth's tectonic and plate boundary evolution over 1.8 billion years. *Geoscience Frontiers*, *15*(6). https://doi.org/10.1016/j.gsf.2024.101922
9. Christensen, U. R. (1985). Thermal evolution models for the Earth. *Journal of Geophysical Research: Solid Earth*, *90*(B4), 2995-3007. https://doi.org/10.1029/JB090iB04p02995
10. Cucchiaro, A., Flament, N., Arnould, M., & Cressie, N. (2025). Large volcanic eruptions are mostly sourced above mobile basal mantle structures. *Communications Earth & Environment*, *6*(1), 538. https://doi.org/10.1038/s43247-025-02482-z
11. Davies, G. F. (1988). Ocean bathymetry and mantle convection: 1. Large-scale flow and hotspots. *Journal of Geophysical Research: Solid Earth*, *93*(B9), 10467-10480. https://doi.org/10.1029/JB093iB09p10467
12. Dhuime, B., Hawkesworth, C. J., Delavault, H., & Cawood, P. A. (2017). Continental growth seen through the sedimentary record. *Sedimentary Geology*, *357*, 16-32. https://doi.org/10.1016/j.sedgeo.2017.06.001
13. Flament, N., Bodur, O. F., Williams, S. E., & Merdith, A. S. (2022). Assembly of the basal mantle structure beneath Africa. *Nature*, *603*(7903), 846-851. https://doi.org/10.1038/s41586-022-04538-y
14. Flament, N., Gurnis, M., Williams, S., Seton, M., Skogseid, J., Heine, C., & Müller, R. D. (2014). Topographic asymmetry of the South Atlantic from global models of mantle flow and lithospheric stretching. *Earth and Planetary Science Letters*, *387*, 107-119. https://doi.org/10.1016/j.epsl.2013.11.017
15. French, S., & Romanowicz, B. A. (2014). Whole-mantle radially anisotropic shear velocity structure from spectral-element waveform tomography. *Geophysical Journal International*, *199*(3), 1303-1327. https://doi.org/10.1093/gji/ggu334

16. Gomi, H., Ohta, K., Hirose, K., Labrosse, S., Caracas, R., Verstraete, M. J., & Hernlund, J. W. (2013). The high conductivity of iron and thermal evolution of the Earth's core. *Physics of the Earth and Planetary Interiors*, *224*, 88-103. https://doi.org/10.1016/j.pepi.2013.07.010
17. Grove, T. L., & Parman, S. W. (2004). Thermal evolution of the Earth as recorded by komatiites. *Earth and Planetary Science Letters*, *219*(3-4), 173-187. https://doi.org/10.1016/S0012-821X(04)00002-0
18. Gubbins, D., Alfe, D., Masters, G., Price, G. D., & Gillan, M. (2003). Can the Earth's dynamo run on heat alone? *Geophysical Journal International*, *155*(2), 609-622. https://doi.org/10.1046/j.1365-246X.2003.02064.x
19. Hassan, R., Flament, N., Gurnis, M., Bower, D. J., & Müller, D. (2015). Provenance of plumes in global convection models. *Geochemistry, Geophysics, Geosystems*, *16*(5), 1465-1489. https://doi.org/10.1002/2015GC005751
20. Hernlund, J. W., & Houser, C. (2008). On the statistical distribution of seismic velocities in Earth's deep mantle. *Earth and Planetary Science Letters*, 265(3-4), 423-437. https://doi.org/10.1016/j.epsl.2007.10.042
21. Herzberg, C., & Gazel, E. (2009). Petrological evidence for secular cooling in mantle plumes. *Nature*, *458*(7238), 619-622. https://doi.org/10.1038/nature07857
22. Heyn, B. H., Conrad, C. P., & Trønnes, R. G. (2020). How thermochemical piles can (periodically) generate plumes at their edges. *Journal of Geophysical Research: Solid Earth*, *125*(6), e2019JB018726. https://doi.org/10.1029/2019JB018726
23. Houser, C., Masters, G., Shearer, P., & Laske, G. (2008). Shear and compressional velocity models of the mantle from cluster analysis of long-period waveforms. *Geophysical Journal International*, *174*(1), 195-212. https://doi.org/10.1111/j.1365-246X.2008.03763.x

24. Jaupart, C., Labrosse, S., Lucazeau, F., & Mareschal, J. (2015). 7.06-temperatures, heat and energy in the mantle of the earth. *Treatise on Geophysics*, *2nd ed.*, *7*, 223-270. https://doi.org/10.1016/B978-0-444-53802-4.00126-3

25. Johansson, L., Zahirovic, S., & Müller, R. D. (2018). The interplay between the eruption and weathering of large igneous provinces and the deep-time carbon cycle. *Geophysical Research Letters*, *45*(11), 5380-5389. https://doi.org/10.1029/2017GL076691

26. Korenaga, J. (2006). Archean geodynamics and the thermal evolution of Earth. *Geophysical Monograph-American Geophysical Union*, *164*, 7. https://doi.org/10.1029/164GM03

27. Korenaga, J. (2008). Urey ratio and the structure and evolution of Earth's mantle. *Reviews of Geophysics*, *46*(2). https://doi.org/10.1029/2007RG000241

28. Korenaga, J. (2017). Pitfalls in modeling mantle convection with internal heat production. *Journal of Geophysical Research-Solid Earth*, *122*(5), 4064-4085. https://doi.org/10.1002/2016jb013850

29. Kustowski, B., Ekström, G., & Dziewoński, A. (2008). Anisotropic shear-wave velocity structure of the Earth's mantle: A global model. *Journal of Geophysical Research: Solid Earth*, *113*(B6). https://doi.org/10.1029/2007JB005169

30. Labrosse, S. (2015). Thermal evolution of the core with a high thermal conductivity. *Physics of the Earth and Planetary Interiors*, *247*, 36-55. https://doi.org/10.1016/j.pepi.2015.02.002

31. Labrosse, S., & Jaupart, C. (2007). Thermal evolution of the Earth: Secular changes and fluctuations of plate characteristics. *Earth and Planetary Science Letters*, *260*(3-4), 465-481. https://doi.org/10.1016/j.epsl.2007.05.046

32. Lay, T., Hernlund, J., & Buffett, B. A. (2008). Core–mantle boundary heat flow. *Nature Geoscience*, *1*(1), 25-32. https://doi.org/10.1038/ngeo.2007.44

33. Li, M., Puetz, S., Condie, K., & Olson, P. (2023). Mantle plume heat flux and surface motion periodicities and their implications for the growth of continental crust. *Earth and Planetary Science Letters*, *611*, 118148. https://doi.org/10.1016/j.epsl.2023.118148

34. Li, M., Zhong, S., & Olson, P. (2018). Linking lowermost mantle structure, core-mantle boundary heat flux and mantle plume formation. *Physics of the Earth and Planetary Interiors*, *277*, 10-29. https://doi.org/10.1016/j.pepi.2018.01.010

35. Li, Y., Deschamps, F., & Tackley, P. J. (2014). Effects of low-viscosity post-perovskite on the stability and structure of primordial reservoirs in the lower mantle. *Geophysical Research Letters*, *41*(20), 7089-7097. https://doi.org/10.1002/2014GL061362

36. MacQueen, J. (1967). Multivariate observations. Proceedings of the 5th Berkeley Symposium on Mathematical Statisticsand Probability,

37. McNamara, A. K., & Zhong, S. (2004). The influence of thermochemical convection on the fixity of mantle plumes. *Earth and Planetary Science Letters*, *222*(2), 485-500. https://doi.org/10.1016/j.epsl.2004.03.008

38. Mittelstaedt, E., & Tackley, P. J. (2006). Plume heat flow is much lower than CMB heat flow. *Earth and Planetary Science Letters*, *241*(1-2), 202-210. https://doi.org/10.1016/j.epsl.2005.10.012

39. Müller, R. D., Dutkiewicz, A., Farkaš, J., Loehr, S., & Merdith, A. S. (2025). Mid-Proterozoic expansion of passive margins and reduction in volcanic outgassing supported marine oxygenation and eukaryogenesis. *Earth and Planetary Science Letters, 672*, 119683. https://doi.org/https://doi.org/10.1016/j.epsl.2025.119683

40. Müller, R. D., Flament, N., Cannon, J., Tetley, M. G., Williams, S. E., Cao, X., Bodur, Ö. F., Zahirovic, S., & Merdith, A. (2022). A tectonic-rules-based mantle reference frame since 1 billion years ago – implications for supercontinent cycles and plate–mantle system evolution. *Solid Earth*, *13*(7), 1127-1159. https://doi.org/10.5194/se-13-1127-2022

41. Nakagawa, T. (2020). A coupled core-mantle evolution: review and future prospects. *Progress in Earth and Planetary Science*, *7*(1). https://doi.org/10.1186/s40645-020-00374-8

42. Nakagawa, T., & Tackley, P. J. (2004). Effects of thermo-chemical mantle convection on the thermal evolution of the Earth's core. *Earth and Planetary Science Letters*, *220*(1-2), 107-119. https://doi.org/10.1016/S0012-821x(04)00055-X

43. Nakagawa, T., & Tackley, P. J. (2008). Lateral variations in CMB heat flux and deep mantle seismic velocity caused by a thermal–chemical-phase boundary layer in 3D spherical convection. *Earth and Planetary Science Letters*, *271*(1-4), 348-358. https://doi.org/10.1016/j.epsl.2008.04.013

44. Nakagawa, T., & Tackley, P. J. (2012). Influence of magmatism on mantle cooling, surface heat flow and Urey ratio. *Earth and Planetary Science Letters*, *329*, 1-10. https://doi.org/10.1016/j.epsl.2012.02.011

45. Nimmo, F. (2015). Energetics of the core. *Treatise on Geophysics*, *8*, 27-55. https://doi.org/10.1016/B978-044452748-6.00128-0

46. Nisbet, E. G., & Fowler, C. M. R. (1983). Model for Archean plate tectonics. *Geology*, *11*(7), 376-379. https://doi.org/10.1130/0091-7613(1983)11<376:MFAPT>2.0.CO;2

47. O'Malley, C. P., Roberts, G. G., Panton, J., Richards, F. D., Davies, J. H., Fernandes, V. M., & Ghelichkhan, S. (2024). Reconciling surface deflections from simulations of global mantle convection. *Geoscientific Model Development*, *17*(24), 9023-9049. https://doi.org/10.5194/gmd-17-9023-2024

48. Olson, P., & Amit, H. (2015). Mantle superplumes induce geomagnetic superchrons. *Frontiers in Earth Science*, *3*, 38. https://doi.org/10.3389/feart.2015.00038

49. Parsons, B., & Sclater, J. G. (1977). An analysis of the variation of ocean floor bathymetry and heat flow with age. *Journal of geophysical research*, *82*(5), 803-827. https://doi.org/10.1029/JB082i005p00803

50. Ritsema, J., Deuss, A., Van Heijst, H., & Woodhouse, J. (2011). S40RTS: a degree-40 shear-velocity model for the mantle from new Rayleigh wave dispersion, teleseismic traveltime and normal-mode splitting function measurements. *Geophysical Journal International*, *184*(3), 1223-1236. https://doi.org/10.1111/j.1365-246X.2010.04884.x
51. Sharpe, H. N., & Peltier, W. (1979). A thermal history model for the Earth with parameterized convection. *Geophysical Journal International*, *59*(1), 171-203. https://doi.org/10.1111/j.1365-246X.1979.tb02560.x
52. Simmons, N. A., Forte, A. M., Boschi, L., & Grand, S. P. (2010). GyPSuM: A joint tomographic model of mantle density and seismic wave speeds. *Journal of Geophysical Research: Solid Earth*, *115*(B12). https://doi.org/10.1029/2010JB007631
53. Sleep, N. H. (1990). Hotspots and mantle plumes: Some phenomenology. *Journal of Geophysical Research: Solid Earth*, *95*(B5), 6715-6736. https://doi.org/10.1029/JB095iB05p06715
54. Stadler, G., Gurnis, M., Burstedde, C., Wilcox, L. C., Alisic, L., & Ghattas, O. (2010). The dynamics of plate tectonics and mantle flow: From local to global scales. *science*, *329*(5995), 1033-1038. https://doi.org/10.1126/science.1191223
55. Tan, E., Leng, W., Zhong, S., & Gurnis, M. (2011). On the location of plumes and lateral movement of thermochemical structures with high bulk modulus in the 3-D compressible mantle. *Geochemistry, Geophysics, Geosystems*, *12*(7). https://doi.org/10.1029/2011GC003665
56. Tappe, S., Smart, K., Torsvik, T., Massuyeau, M., & de Wit, M. (2018). Geodynamics of kimberlites on a cooling Earth: Clues to plate tectonic evolution and deep volatile cycles. *Earth and Planetary Science Letters*, *484*, 1-14. https://doi.org/10.1016/j.epsl.2017.12.013

57. Van Der Meer, D. G., Spakman, W., Van Hinsbergen, D. J., Amaru, M. L., & Torsvik, T. H. (2010). Towards absolute plate motions constrained by lower-mantle slab remnants. *Nature Geoscience*, *3*(1), 36-40. https://doi.org/10.1038/ngeo708

58. Zhong, S. (2006). Constraints on thermochemical convection of the mantle from plume heat flux, plume excess temperature, and upper mantle temperature. *Journal of Geophysical Research: Solid Earth*, *111*(B4). https://doi.org/10.1029/2005JB003972

59. Zhong, S., McNamara, A., Tan, E., Moresi, L., & Gurnis, M. (2008). A benchmark study on mantle convection in a 3-D spherical shell using CitcomS. *Geochemistry, Geophysics, Geosystems*, *9*(10). https://doi.org/10.1029/2008gc002048

Supplementary material

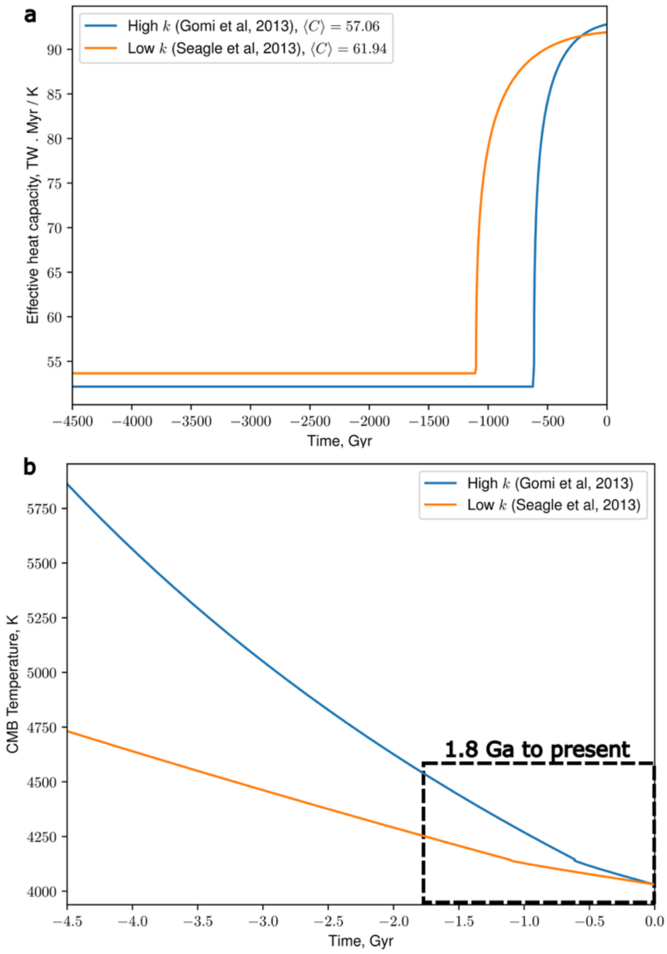

Figure S1. a, Evolution of the effective total heat capacity of Earth's core. **b**, Evolution of the CMB temperature derived from a coupled core-mantle thermal evolution model modified from Labrosse (2015). The orange line shows the result from Seagle et al. (2013), and the blue line shows the result from Gomi et al. (2013), in which the thermal conductivity was larger.

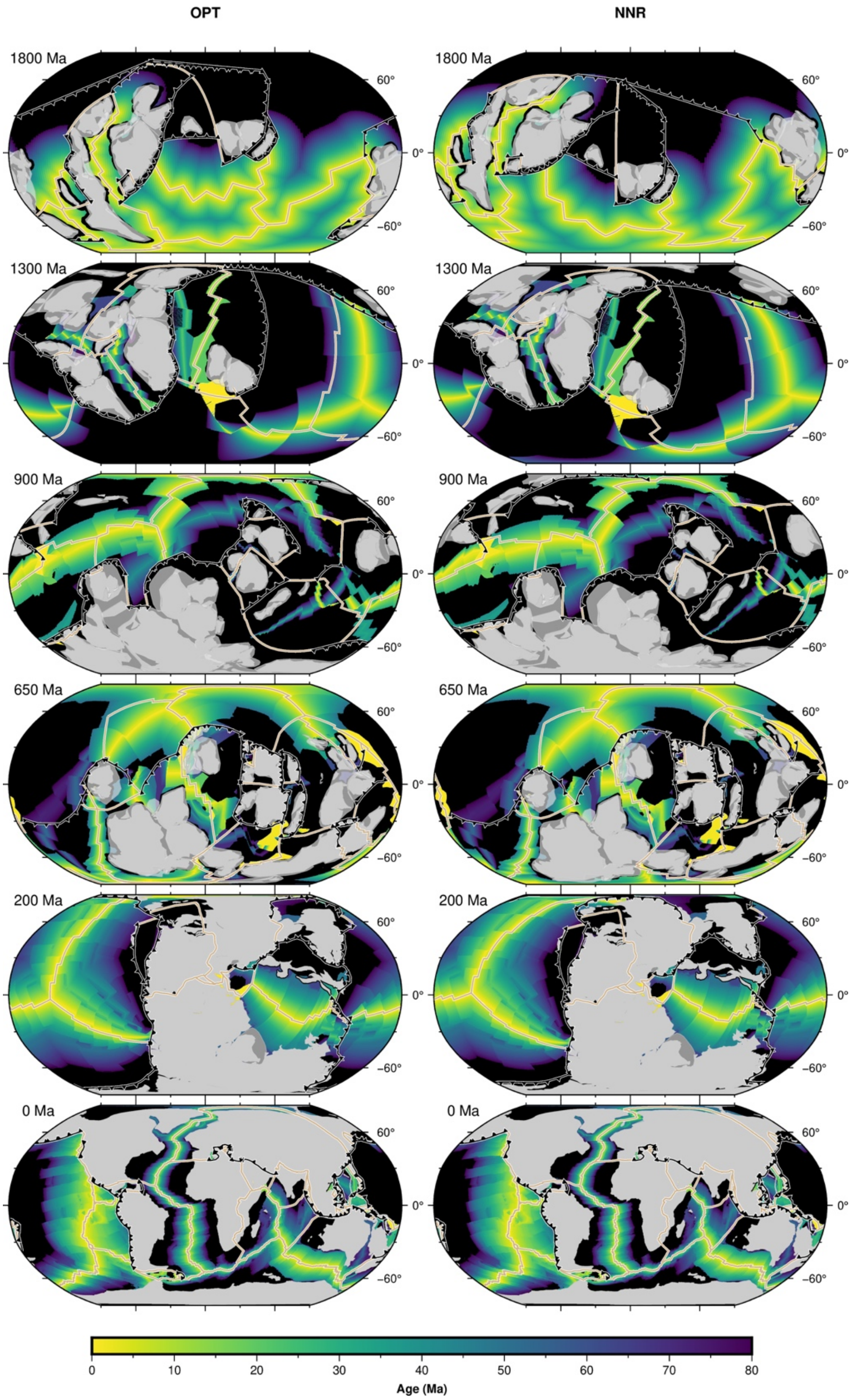

Figure S2. Plate configurations in C24 at 1800 Ma, 1300 Ma, 900 Ma, 650 Ma, 200 Ma, and 0 Ma for the optimized reference frame (OPT; left column) and no-net-rotation reference frame (NNR; right column). The background shows seafloor age. Plates are represented by grey blocks. Lines with triangles on the overriding plate represent convergent plate boundaries and solid lines represent divergent plate boundaries.

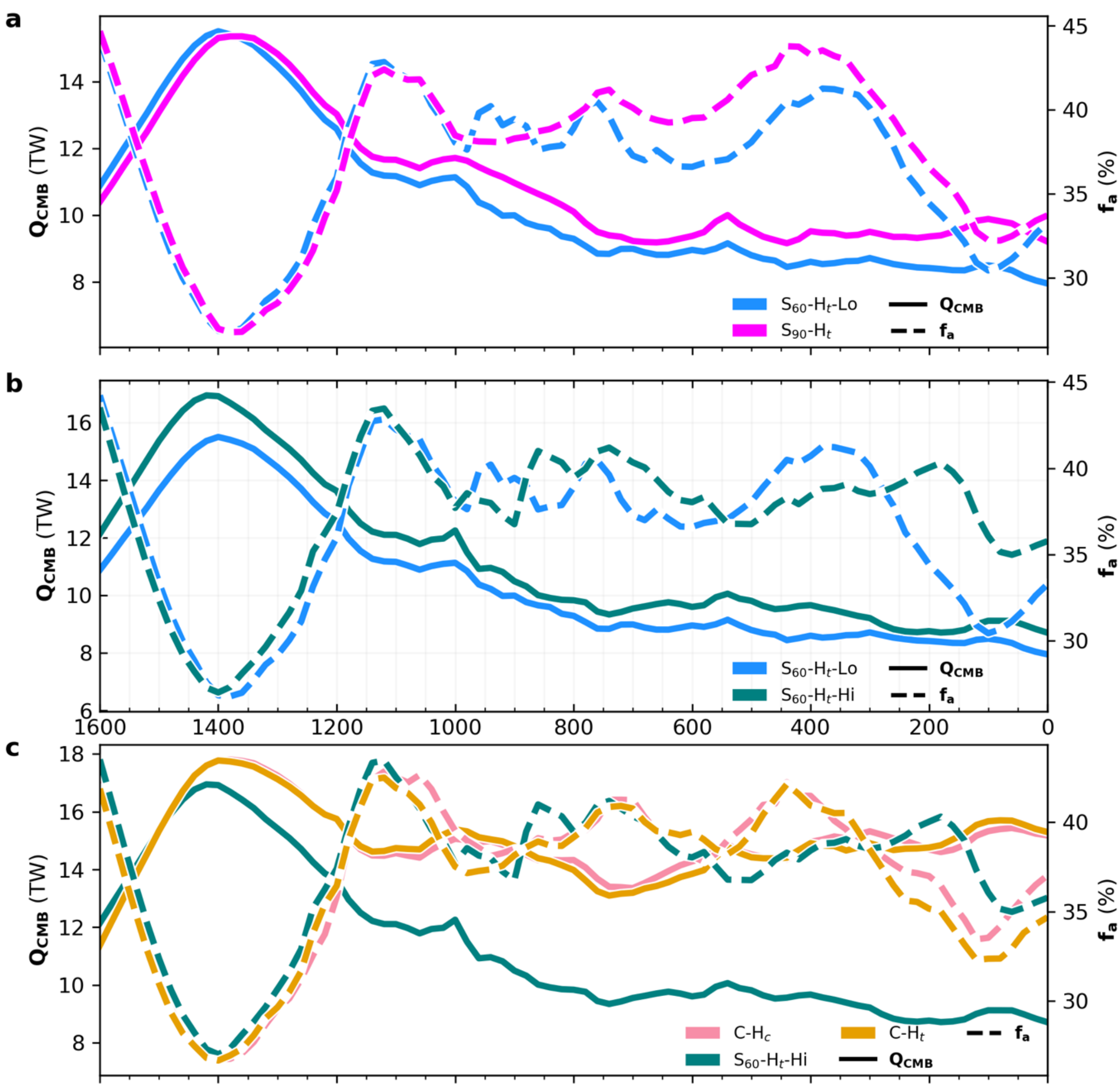

Figure S3. CMB heat flow Q_{CMB} and BLOBS fractional area f_a as a function of time. **a)** Results for cases S_{60}-H_t-Lo, and S_{90}-H_t, illustrating the effects of self-consistent T_{CMB}, with different core thermal conductivity. **b)** Results for cases S_{60}-H_t-Lo, and S_{60}-H_t-Hi, illustrating the effects of greater convective vigour. **c)** Results for cases C-H_c, C-H_t, and S_{60}-H_t-Hi, illustrating the effects of basal cooling and cooling from the interior. Solid lines show Q_{CMB} and dashed lines represent f_a. Model cases are color-coded.

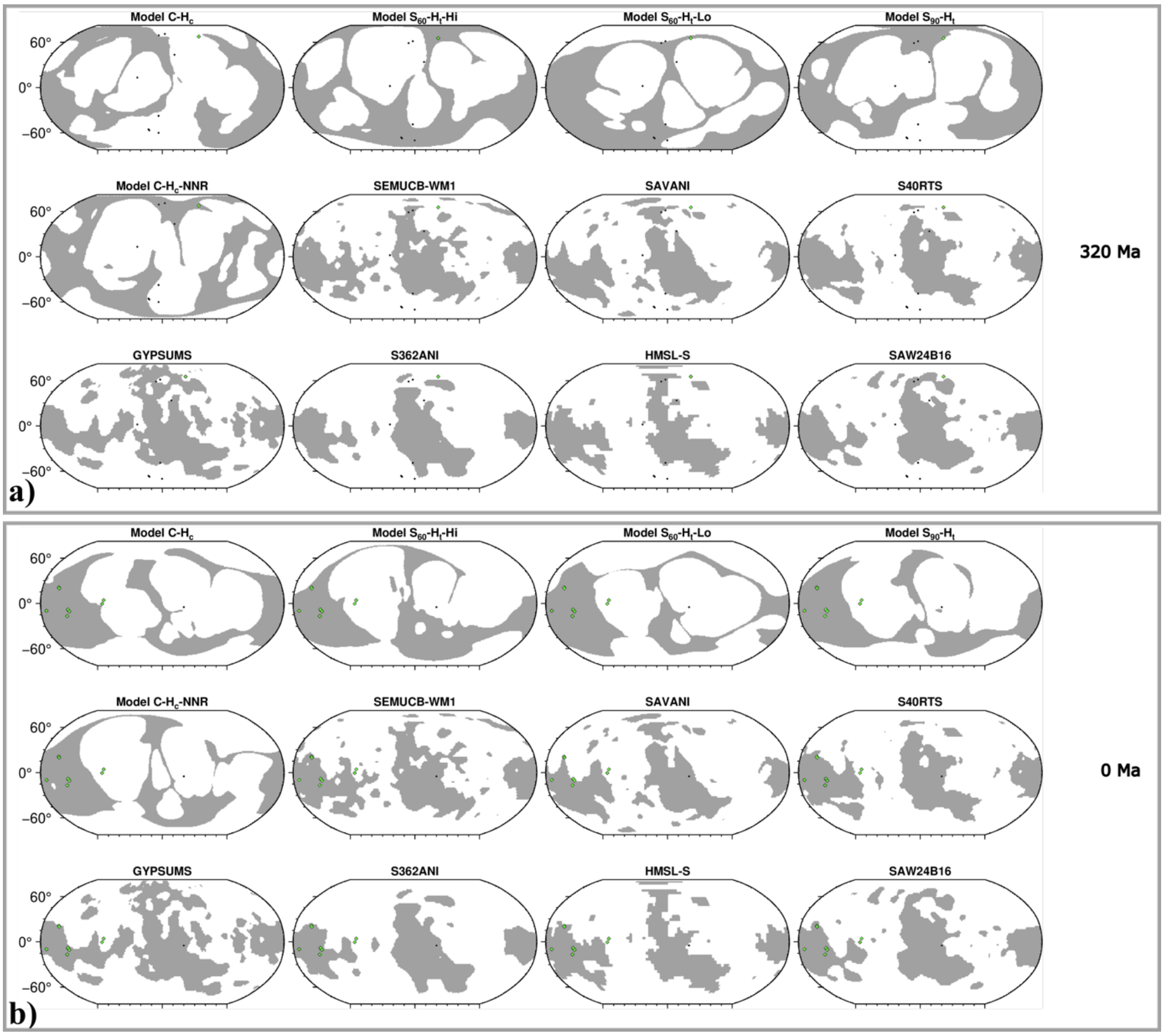

Figure S4. Model cluster maps (1000-2800 km depth), and volcanic eruptions at 320 Ma (**a**) and present-day (**b**), together with present-day seismic tomographic model cluster maps. The grey regions denote BLOBS. The green diamonds and black dots represent reconstructed LIP locations from Johansson et al. (2018) and kimberlite locations from Tappe et al. (2018).

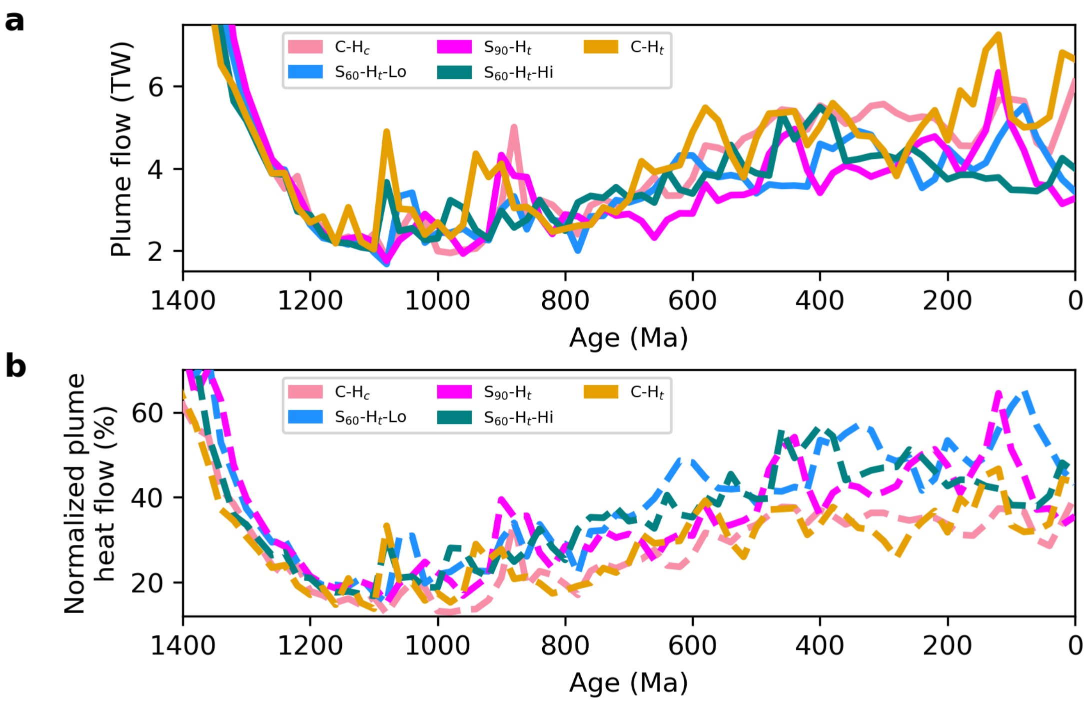

Figure S5. Evolution of plume heat flux predicted by mantle flow models in optimized mantle reference frame. **(a)** Heat flux carried by lower mantle plumes at 1,040 km depth, Q_{plume}, since the end of the transient phase for model cases C-H$_c$, C-H$_t$, S$_{60}$-H$_t$-Lo, S$_{90}$-H$_t$, and S$_{60}$-H$_t$-Hi. **(b)** Plume heat flux at 1,040 km depth normalized to CMB heat flow. Different models are represented with different colours.

Table S1. Radiogenic heat production.

Isotope	h_n	λ_n(1/Gyr)
^{238}U	0.372	0.155
^{235}U	0.0164	0.985
^{232}Th	0.43	0.0495
^{40}K	0.181	0.555